Precision Prediction of Microbial Ecosystem Impact on Host Metabolism Using Genome-Resolved Metagenomics

Mohamed Mohssen†[1,2,3,4], Ahmed A. Zayed†[2,3,4], Kristina A. Kigerl†[5,6], Jingjie Du[2,¥], Garrett J. Smith[2,3], Jan M. Schwab[5,6], Matthew B. Sullivan*[1,2,3,4,7] and Phillip G. Popovich*[3,5,6]

1 The Interdisciplinary Biophysics Graduate Program, The Ohio State University, Columbus, Ohio 43210, USA
2 Department of Microbiology, The Ohio State University, Columbus, Ohio 43210, USA
3 Center of Microbiome Science, The Ohio State University, Columbus, Ohio 43210, USA
4 EMERGE Biology Integration Institute, The Ohio State University, Columbus, Ohio 43210, USA
5 Department of Neuroscience, The Ohio State University Wexner Medical Center, Columbus, OH, 43210, USA
6 Belford Center for Spinal Cord Injury, The Ohio State University Wexner Medical Center, Columbus, OH, 43210, USA
7 Department of Civil, Environmental and Geodetic Engineering, The Ohio State University, Columbus, OH 43210, USA
¥ Current Address: Division of Nutritional Sciences, Cornell University, Ithaca, NY, 14850, USA
† These authors contributed equally
* Correspondence: phillip.popovich@osumc.edu and sullivan.948@osu.edu

Abstract

Microbes drive ecosystem function through their physical interactions and metabolic transformations. However, since microbiomes are ecologically and metabolically interconnected, it is challenging to predict emergent ecosystem responses once the microbiome is disturbed. While it is widely acknowledged that mammalian gut dysbiosis influences host metabolism, mechanistic links that predict these effects are understudied. This study employs a genome-resolved eco-systems biology approach, using a high-resolution 'spinal cord-gut axis' model system and dataset, to predict how dysbiotic gut metabolism impacts overall mammalian health. By scaling and combining temporally resolved network analytics and consensus statistical methods, key microbial species were identified that predict overall host physiology and presumably control the gut ecosystem. *In silico* validation by pathway-centric functional analyses and comparative genomics revealed that key bacteria, sometimes exclusively, encode functions linking microbial and host metabolisms. Notably, spinal-mediated disturbances in the ecosystem shifted gut microbial nitrogen metabolism from urease- to amino acid-dependent pathways, with patterns that varied by host sex and bacterial species. Overall, this research challenges the traditional paradigm that only the host maintains whole-body nitrogen balance and instead invokes the microbiome as an environmentally-sensitive regulatory organ that can dictate health or disease by influencing mammalian whole-body elemental balance.

Introduction

Earth systems are inhabited by microbes that perform key elemental transformations including carbon[1,2] and nitrogen[3] cycling. In these systems, ecological context is critical for understanding microbiota functioning, with genome-resolved metagenomic analyses being the gold standard for capturing key, niche-defining functions that often evolve faster than marker-gene-correlated core functions[4–13]. The gut microbiome is a dynamic ecosystem where microbes constantly exchange and compete for metabolites and other molecules[14,15]. Therefore, assessing gut microbiota in isolation (i.e., a single taxon at a time via all-vs-all pairwise testing) cannot account for complex interactions among microbiota. The result is that translating taxon abundances and gene lists into ecosystem-level biological understanding remains a grand challenge in the life sciences.

Unlike microbes, mammals cannot acquire or "fix" nitrogen from the atmosphere even though mammalian physiology is typically correlated with nitrogen balance[16], where net nitrogen gain and loss are associated with health and disease, respectively. Instead, mammals obtain nitrogen mostly from dietary proteins, which they then catabolize into nitrogen-rich compounds like amino acids and ammonia. Although the liver is the primary site where protein is metabolized and ammonia detoxified, intestinal bacteria can also participate in nitrogen metabolism. For example, albeit typically treated as a "black box", urea nitrogen salvaging (UNS) by gut microbes likely plays an appreciable role in mammalian nitrogen metabolism[17,18].

Here we sought to establish a data-driven workflow to better identify emergent ecosystem properties, including precise microbial contributions to host whole-body nitrogen metabolism, and to apply it to a biomedically-relevant dataset to improve our understanding of host-microbiome dynamics and functioning in health and disease. To do this, we focused on neurological impairment (NI) as a gut ecosystem "environmental" challenge[19,20] that can change host nitrogen metabolism[16,21]. We previously established a well-controlled spinal cord-gut axis murine model system[22] that represents NI and includes high-resolution gut metagenome temporal sampling, and manually reconstructed carbon-based microbial metabolic connectivity in the gut ecosystem to inform microbe-microbe interactions. Using this model, we here develop a systematic workflow to investigate microbe-host interactions using (i) cross-validated eco-systems biology and machine learning to identify key ecosystem-impacting microbial taxa, and (ii) consensus genome-resolved, pathway-centric analyses to elucidate metabolism-based mechanisms underpinning these ecosystem impacts. Application of this data-driven approach highlights key microbial taxa and metabolic pathways influencing host nitrogen metabolism and provides insights into potential therapeutic targets for future *in vivo* validation.

Emergent gut microbial networks predict host physiology

To evaluate ecosystem-contextualized microbiome-host metabolic interactions, a well-curated model system and microbiome dataset are needed. To this end, we leveraged the curated Mouse B6 Gut Catalog (MB6GC)[22], which includes 263 dereplicated metagenome-assembled genomes (MAGs) recovered from fecal and cecal samples temporally obtained from male and female mice with graded levels of NI caused by spinal lesions at mid- (T10) or high- (T4) thoracic spinal levels. Such lesions partially or completely disrupt neural control over the gut. Mice receiving spinal surgery but without a spinal cord lesion served as a control group ("Lam") (see [22] for full study design). These MAGs, which represented the *in situ* gut microbial community quite well (i.e., they recruited ~80% of the total metagenomic reads), were quantified over 6 months across groups and evaluated against a standardized scale of neurological function in mice (Basso Mouse Scale, or BMS, for locomotion[23]) as a proxy for overall mouse physiological state.

To analyze these data considering the fuller microbial community context, we move beyond pairwise statistical approaches and apply an eco-systems biology approach (*sensu* [24]). This approach uses MAG-based relative abundance data to organize the microbial community into predictably interacting (e.g., competing or cross-feeding) sub-communities of co-occurring MAGs via weighted gene/genome correlation network analysis (WGCNA)[25]. Longitudinal sample-dependencies were accounted for by generating six independent networks – one for each timepoint across 6 months following NI (see **Fig. 1A**, **Fig. S1**, and "*WGCNA Analysis"* in the **Methods** for more details). The resultant initial networks were power-transformed to identify robust subnetworks (i.e., modules) meant to represent microbial sub-communities whose members co-vary and therefore possibly interact. Each subnetwork was then correlated with host neurological function (BMS) scores such that member taxa of correlating subnetworks could be analyzed via leave-one-out (LOO) cross-validation to identify members critical for these associations. Specifically, LOO cross-validation via partial least square (PLS) regression analysis assigned variable importance in projection (VIP) scores to each taxon to identify key MAG(s) within each emergent subcommunity (see **Fig. 1A** inset), in effect linking member taxa with host health. We generalized this cross-validated PLS-VIP approach to all emergent sub-communities, using the consensus of multiple statistical techniques, cross-validation methods, and manual inspection (see "*WGCNA analysis*" in **Methods**) to identify key MAGs inferred to drive ecosystem changes, hereafter named "PLS-VIP MAGs". Only MAGs from male mice networks met the strict criteria of the PLS-VIP MAGs (see details on sex-specific taxon and functional changes in[22].

Application of this workflow to MB6GC MAGs derived from mice with or without NI revealed the following. For "normal", non-perturbed gut ecosystems in healthy mice with intact

spinal cords, this workflow revealed no emergent sub-communities at baseline (i.e., Day 0) – as expected from similar microbial communities. However, subsequent time points revealed multiple emerging sub-communities after NI (**Fig. 1A**). In total, 19 consensus PLS-VIP MAGs were identified that likely control ecosystem dynamics and function after disrupting spinal cord-gut crosstalk (**Fig. 1**). Of these 19 PLS-VIP MAGs (**Fig. 1B-C**), 11 MAGs from the Firmicutes_A phylum increased in abundance (Group 1 MAGs), whereas 8 MAGs from 4 separate phyla decreased (Group 2 MAGs). Six of the 19 MAGs had strong associations with health or disease states based on prior studies, and of these six MAGs, five decreased (*Lactobacillus Johnsonii*, Turicibacter sp002311155, *Parasutterella excrementihominis*, CAG-485 sp002362485, and CAG-873 sp910577315) and one increased (Acetatifactor sp003612485) after lesioning the spinal cord. Published data indicate that these microbes can significantly affect host physiology: (i) *L. johnsonii* enhances gut barrier integrity[26] and gut mucosal immunity[27], and reduces plasma total cholesterol levels[28]; (ii) Turicibacter sp002311155 was reduced after murine lung cancer in mice[29] and strains of the Turicibacter genus differentially modify bile acids and lipid metabolism[30]; (iii) *P. excrementihominis,* a core component of human and murine microbiomes with roles in bile acid maintenance and in cholesterol and tryptophan metabolism, is reduced by high-fat-diet[31]; (iv) CAG-485 sp002362485 (recently proposed as "*Sangeribacter muris*" and biochemically characterized in[32]) is one of the most dominant and prevalent species in the murine gut and may protect from intestinal colitis[32]; (v) similar to *P. excrementihominis*, CAG-873 sp910577315 decreased after high-fat-diet in mice[33], whereas (vi) Acetatifactor sp003612485 levels were positively correlated with plasma metabolites implicated in cardiovascular diseases[34].

In summary, 19 species-level MAGs were identified that best predict host physiological state – 6 already linked to health and disease in other model systems and 13 newly identified here.

Inferring microbial community metabolic output driven by key network-emergent taxa

Next, we asked how PLS-VIP MAGs might impact host (patho)physiology. Answering this question is challenging since, within complex ecosystems like the gut, microbes are often functionally redundant (i.e., sharing metabolic blueprints[35,36]) and metabolically connected (i.e, cross-feeding[37]). Hence, we analyzed PLS-VIP MAGs' functional potential in the context of the entire gut microbial community (PLS-VIP MAGs + other community members) metabolism. Specifically, we estimated relative abundances of microbial metabolic functions (see Methods and **Fig. 2A**) and identified metabolic pathways fulfilling two criteria: (i) those with relative abundances that significantly changed in mice with NI (vs. sham controls) taking into account *all*

149 recovered MAGs encoding these pathways (**Fig. S2-3**), and (ii) those that were differentially
150 encoded between PLS-VIP MAGs that increased or decreased in mice with NI as determined by a
151 statistical enrichment analysis – see (**Fig. S4** and **Methods**). To identify PLS-VIP MAG-dependent
152 pathway-level changes that are not functionally compensated by other community members (i.e.,
153 pathways not encoded by non-PLS-VIP MAGs or encoded only in rare non-PLS-VIP MAGs),
154 only pathways meeting both criteria were analyzed further.

155 Identifying PLS-VIP MAG-dependent pathways proceeded as follows. *First*, Anvi'o[38] was
156 used to functionally annotate (see "*Pathway identification"* in **Methods**) all 263 MAGs against
157 the KEGG database and organize these annotations (KEGG Ortholog [KO] numbers) into
158 hierarchical KEGG modules that represent partial or complete metabolic pathways. *Second*,
159 module completeness (*sensu* [39], see **Methods**) was estimated per MAG from the constituent KEGG
160 genes present in it (**Fig. S4A**). *Third*, using abundances of complete modules, a time-resolved,
161 whole-community differential analysis was performed (see "*Fold-change calculation for*
162 *visualizing pathways"* in **Methods**). This analysis revealed that 26 modules (**Fig. 2B**), as defined
163 by hierarchical clustering (**Fig. S2A**; see all modules in **Fig. S2-3**), encompassed all observed
164 changes in mice with NI, regardless of spinal lesion level or sex. Thus, these 26 modules represent
165 *whole-community* metabolic changes. *Finally,* and independently, a generalized linear model
166 within Anvi'o[40] (see "*Pathway enrichment analysis*" in **Methods**) was used to quantify the
167 enrichment of each KEGG module across Group 1 and 2 PLS-VIP MAGs, i.e., those that increased
168 or decreased, respectively. This enrichment analysis identified 52 modules as differentially
169 encoded by the two groups of PLS-VIP MAGs (**Fig. S4B**).

170 The intersection of these 52 PLS-VIP MAG-level and 26 whole community-level findings
171 identified 19 complete VIP-driven modules (**Fig. 2B**) that represent abundance-based microbial
172 metabolic changes in mice with NI. We hereafter refer to these modules as "Community VIP
173 (cVIP)-driven modules". Of these, six modules (**Fig. 2B**) belong to interconnected themes of
174 microbial metabolism critical for host nitrogen metabolism, namely ammonia/urea and amino
175 acid/polyamine metabolisms. Given this, we discuss how these six changing microbial metabolic
176 pathways could affect animals and people with spinal cord dysfunction and other diseases of the
177 CNS.

178 Gut microbial nitrogen metabolism disruption by 179 neurological impairment

180 Among the 19 cVIP-driven modules, one module involved in bacterial fixation of inorganic
181 nitrogen (dissimilatory nitrate reduction, via nitrite, to *ammonia*, hereafter DNRA; KEGG module
182 M00530) was significantly reduced in mice with NI (**Fig. 2B**) and was solely encoded by *P.*

183 *excrementihominis* among the PLS-VIP MAGs (**Fig. S4**). DNRA enables the retention of scarce
184 nitrogen as soluble ammonia in organic-rich and anoxic ecosystems[41] and is considered a major
185 pathway for nitrate reduction by bacteria in rumen and human intestine[42–45].

186 We also observed in mice with NI, a significant reduction in the bacterial organic nitrogen
187 pathway UNS involved in degrading *urea* to ammonia via urease genes (see **Introduction**). We
188 inspected urease-encoding bacteria by manual reconstruction of the urease pathway from single-
189 gene annotations of its constituent genes (*sensu* [46]) as it was absent from the KEGG hierarchy, and
190 we then genome-contextualized this pathway (see analysis of cVIP-driven modules above). This
191 revealed that, among PLS-VIP MAGs, 100% of the urease pathway was encoded by only CAG-
192 485 sp002362485 and CAG-873 sp910577315. These two MAGs were highly dominant as their
193 collective median relative abundances represented >35% or ~16-20% of the microbial community
194 in healthy (i.e., Lam) or male mice with NI, respectively (**Fig. 3A-B**). Further, only four other
195 MAGs, collectively accounting for <1% of the entire microbial community, encoded this complete
196 pathway (**Fig. 3B**). Notably, comparative genomics revealed that other MAGs from the same
197 family of the two urease-encoding PLS-VIP MAGs (Muribaculaceae) lacked urease genes (**Fig.
198 3A**). This suggests relatively recent functional trait evolution in CAG-485 sp002362485 and CAG-
199 873 sp910577315, which would be missed using KEGG hierarchy-based indirect metabolic
200 predictions from marker-gene analyses[47]. The relative abundance of these two MAGs was less
201 prominent in healthy female mice (baseline <20% median relative abundance) and less affected
202 by NI. Instead, other non-urease-encoding Muribaculaceae (i.e., Duncaneilla MAGs) dominated
203 the gut of healthy female mice and were significantly decreased in female mice with NI (**Fig. 3B**).
204 These data suggest sex-specific microbiota-host metabolic interactions could influence outcome.
205 This is an important consideration when the decision to use only one sex is based purely on
206 experimental logistics and feasibility (e.g., cost, ease of handling, post-operative care, etc.).

207 Finally, our data revealed significant spinal cord-dependent changes in cVIP-driven
208 modules encoding *amino acids* and *polyamines*. cVIP-driven modules encoding the amino acids
209 tyrosine and phenylalanine were significantly reduced (**Fig. 2B**, **Fig. 4**). Among PLS-VIP MAGs,
210 only *P. excrementihominis* encoded 100% of these pathways (**Fig. S4**). Conversely, other cVIP-
211 driven modules increased significantly in mice with NI. Those modules encode *polyamine*
212 precursors – the amino acids arginine and ornithine – as well as polyamines themselves (**Fig. 2B**,
213 **Fig. 4**). Taxonomically, these biosynthesis pathways were well-represented in Group 1 PLS-VIP
214 MAGs (increasing after NI; 2/11 for polyamine, 11/11 for arginine, and 10/11 for ornithine), but
215 were sparse in Group 2 PLS-VIP MAGs (decreasing after NI; 0/8 for polyamine, and 2/8 for
216 arginine and ornithine) (**Fig. S4**).

Discussion

This work provides a scalable genome-resolved, functionally-contextualized eco-systems biology analytical roadmap that can help the field move beyond simple correlations between individual microbes and host health, which fail to consistently infer microbe-host interactions in complex system like the gut[48]. The first step in this workflow scales up and semi-automates eco-systems biology approaches developed in another complex ecosystem (i.e., the oceans[24]) to organize taxa or metabolic functions to assess interacting subsets, evaluate their predictive power of ecosystem properties (e.g. carbon flux in the oceans or disease status in mammals), and cross-validate them to assess the specific taxa or functions that are most important to these predictions. Our upgraded workflow makes it possible to apply this eco-systems biology approach to longitudinal datasets, controlling for temporal dependencies[49]. The second advance in our workflow was to curate identified taxa (i.e., PLS-VIP MAGs) from the first step by removing redundant ones across longitudinally differentiated networks and examining the consistency of each taxon's temporal abundance patterns. Finally, the third advance in this workflow was to mechanistically and functionally contextualize changes in consensus PLS-VIP MAGs. This was done by leveraging genome-resolved "complete"-pathway functional signals from multiple data streams – i.e, the consensus of PLS-VIP MAG-based functional enrichment analysis and whole-community-based hierarchical clustering of functions. These combined analyses reduce reliance on pairwise statistical inferences, focusing instead on identifying key taxa and complete pathways to assess their functions and impacts within community-scale interactions.

Applied to a large-scale dataset from mice with and without neurological impairment, our workflow revealed 19 key whole-community-stabilizing gut bacterial members (i.e., PLS-VIP MAGs; **Fig. 1**) that are regulated by the spinal cord. Further, our data-driven approach, supported by consensus statistical methods (**Fig. 2A**), identified 19 microbial metabolic pathways that drive microbial ecosystem dynamics in the gut of mice with NI (**Fig. 2B**). We highlight six of these pathways together with an *ad hoc* reconstructed UNS pathway – all centered around nitrogen metabolism – that suggest microbiota play a larger role in influencing nitrogen balance in the host than previously recognized. Two specific, clinically-relevant examples follow.

First, NI, caused by selective spinal cord lesions in male mice, significantly reduced the abundance of gut bacterial MAGs encoding ammonia biosynthesis and urea degradation pathways (**Fig. 3**), presumably reducing ammonia and elevating urea microbial production in the host. Published data has hinted at sex-specific nitrogen metabolism. For example, in male mice, stress-induced reductions in urease-positive gut bacteria caused ammonia levels to significantly drop in colon and blood, which was also associated with depressive-like behaviors and dysfunctional neurotransmission[46]. We posit that similar system-wide changes are expected whenever there is

252 spinal cord dysfunction, which occurs in virtually all neurological diseases[50–56]. Indeed,
253 maintaining organismal homeostasis requires the sympathetic nervous system, which originates in
254 the spinal cord. Since most sensory information relayed from peripheral tissues enters through the
255 spinal cord or later becomes integrated in the spinal cord, any type of perturbation in the nervous
256 system will impair neurotransmission through the spinal cord and the ability of the spinal cord to
257 control systemic organs, including the gut. After traumatic spinal cord injury (SCI), chronic
258 reduction of gut urease-positive bacteria may contribute to post-injury uremia – a common
259 comorbidity in SCI patients that, so far, has been solely attributed to paralysis-dependent muscle
260 catabolism and impaired renal function (based on male rat data[57]). Dysfunctional gut microbial
261 urea/ammonia metabolism, as observed in our data, could also explain why negative nitrogen
262 balance in SCI patients cannot be overcome with aggressive nutritional intervention[58,59]. While
263 more work is needed to explain why experimentally-induced changes in gut urease-positive
264 bacteria vary by sex, we posit that lower levels of these bacteria in female mice indicate a lower
265 dependency on the gut microbiome as an ammonia source, compared to males. This hypothesis is
266 supported by data showing that the rate of ammonia generation and recycling in the kidney are
267 greater in female compared to male mice[60,61].

268 Second, NI also significantly changed the abundance of gut bacterial MAGs encoding
269 health-critical aromatic and non-aromatic amino acids and polyamines. Biosynthetic pathways of
270 aromatic amino acids tyrosine and phenylalanine were reduced after NI. These amino acids can
271 enter the circulation from the gut then bypass the blood-brain or blood-spinal cord barriers where
272 they are used to synthesize dopamine and (nor)epinephrine, which are neurotransmitters critical
273 for normal neurological function[62]. Biosynthetic pathways for the non-aromatic, semi-essential
274 amino acid arginine and for polyamines increased in mice with NI. Because arginine is used as a
275 precursor for synthesizing polyamines and proteins[63], an increase in gut microbial arginine
276 biosynthesis, or its precursor ornithine, might benefit the host[64,65]. However, literature from murine
277 SCI models showed that an arginine boost may promote inflammation and tissue injury (e.g.,
278 neurological recovery was impaired if mice received arginine supplements and neurological
279 function improved if arginine was depleted[66,67]). Similarly, although polyamines are critical for
280 cell growth and viability in mammals[65], they have been shown to be elevated in serum of uremic
281 patients[68]. Given this conflicting literature, we posit that (i) elevated polyamine levels contribute
282 to urea accumulation as the polyamine biosynthetic process releases urea and creates agmatine
283 and/or putrescine (**Fig. 4**), and (ii) the two products (agmatine and putrescine) could play both
284 beneficial and harmful roles in the context of disease or injury to the CNS[69,70].

285 Based on the data presented, we propose that the increase in blood urea associated with
286 neurological injury or disease is due to microbial shifts linked to the disruption of spinal cord-gut
287 communication. These shifts include (i) a reduction of bacteria encoding urease (particularly in

males) and neurotransmitter precursors, and (ii) an increase in bacteria encoding health-critical amino acids and polyamines. Shifting from pre-dysbiotic microbes synthesizing ammonia as their nitrogen source to dysbiotic microbes synthesizing amino acids is consistent with previous reports showing similar metabolic patterns when Clostridia are dominant within the microbial community[71]. Indeed, our data indicate that all 11 PLS-VIP MAGs that increase in the gut of mice with NI belong to the class Clostridia, as opposed to only 3 out of the 8 PLS-VIP MAGs decreasing in these same mice. Finally, our work shows that understanding community context and interactions is essential when making inferences about local and systemic effects of the gut microbiome (e.g., urea and ammonia balance in the host). Further, the PLS-VIP MAGs identified here are presumably the main drivers of this microbial metabolism, with little to no compensation by rare community members, providing a list of probiotic targets to be experimentally verified in future studies.

Conclusions

This report suggests that spinal cord-mediated altered gut microbial metabolic potential impacts host nitrogen metabolism. These results were obtained using an improved, hypothesis-free, data-driven approach that required no *a priori* assumptions or knowledge and used scalable and genome-informed analytics. Some taxa are newly predicted to affect host metabolism even though they are seldom linked to neurological disorders and rarely, if ever, considered to be under the influence of spinal sympathetic networks. If validated in relevant neurological disease models, these taxa would represent broadly impactful probiotics due to their functioning (shown here) and ubiquity as part of the core gut microbiome[72,73]. Important to such follow-up work will be recapitulating the community context, such as cross-feeding partners and competing niches, that is inherent in natural microbiomes and captured in our analytics. For CNS diseases, progress towards this goal could leverage microbes as therapeutics to restore nitrogen balance to treat symptoms that are characteristic of CNS diseases with impaired spinal cord-gut communication (e.g., stroke, spinal injury, multiple sclerosis, and neurodegenerative diseases)[58,59]. Indeed, recent data show that restoring one PLS-VIP MAGs can prevent the onset of metabolic dysfunction caused by SCI[22]. More broadly, however, this report provides a roadmap for addressing a grand challenge in microbiome science whereby microbiota and their functions are more mechanistically linked with their environmental[1] and/or host[13,74–76] contexts. Given the challenges of *in-vivo*-representative synthetic communities experiments (e.g., including all interacting partners[77], we query the natural community interactions across different 'environmental' conditions. We do this by shifting from global pairwise predictions about microbial functions based on conserved, slow-evolving marker genes (e.g., 16S rRNA genes) – which are likely evolutionarily out of sync with many ecological traits[4–13] – towards genome-, population-structure-[11] and community-informed

323 functional predictions. In this way, our data-driven discovery process can better predict the fast-
324 evolving, niche-defining traits that structure ecosystems and that can vary significantly within
325 genera and species[9,13] in a community. Such analytical advances, alongside improved community
326 metabolic modeling approaches to assess unintended consequences[78,79], will expedite the
327 development of systems-level knowledge, which traditionally requires years to achieve but is
328 critical to more fully realize the potential for microbiome engineering as a precise and context-
329 specific therapeutic for personalized medicine.

330

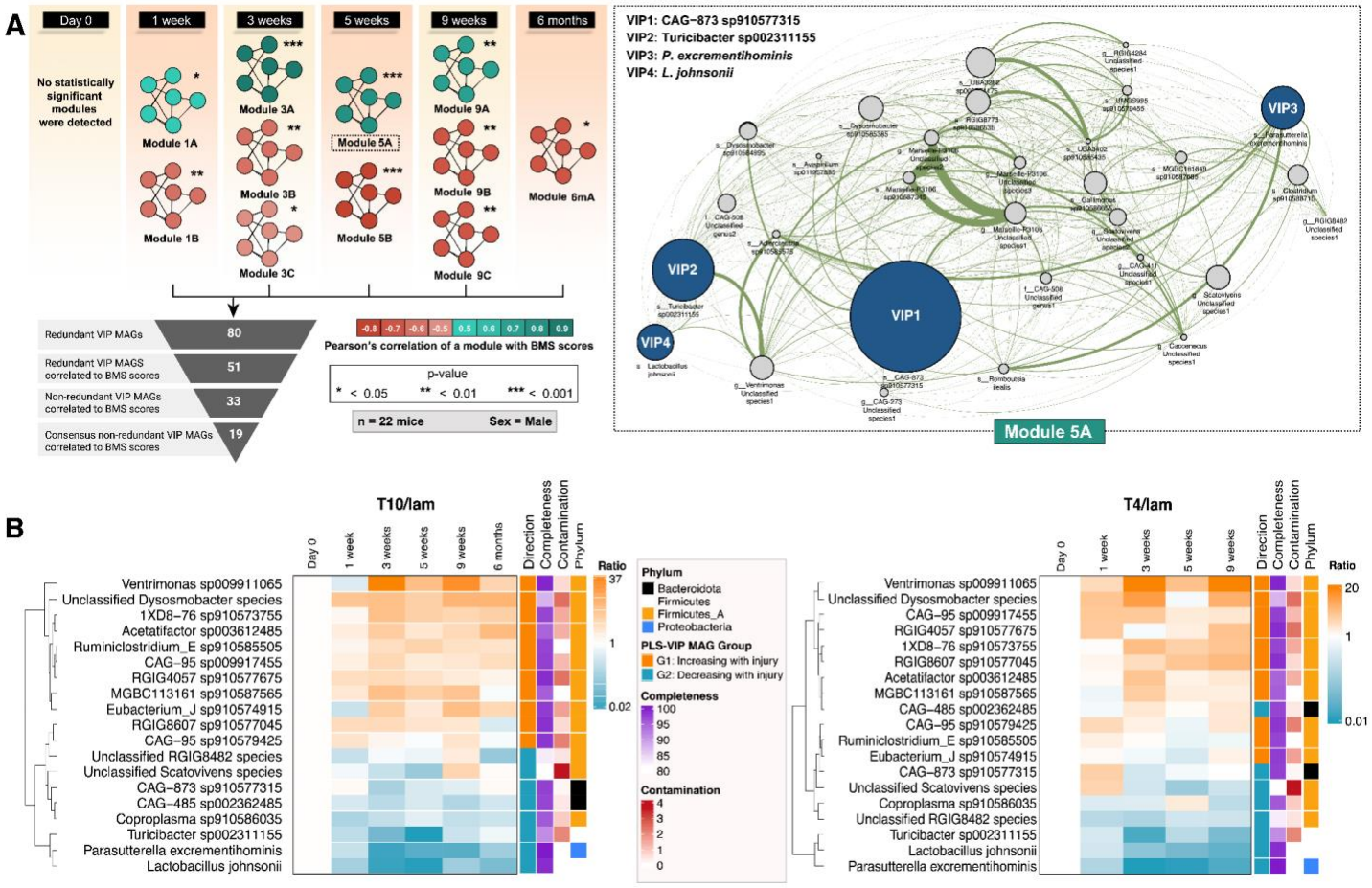

Fig. 1. Eco-systems biology distillation of interacting microbiota into host-impacting drivers.

(A) A schematic of statistically significant sub-communities (in shades of green and red) at each timepoint (see "*WGCNA Analysis*" in **Methods** and **Fig. S1** for details) correlated against 6-months-post-injury BMS score (colored for positive correlations and red for negative correlations and *p*-values as indicated). The modules (subnetworks) are named after the variable time-points: Module 1A = a module emerging at week 1, etc. The inverted pyramid (bottom) shows the number of MAGs filtered at each step of the workflow, distilled to 19 consensus MAGs after accounting for statistical anomalies and normal (i.e., Lam) microbiome drift over time (see "*Inspection of PLS-VIP MAGs*" in **Methods** for details). Inset (right) shows a network visualization of one module (i.e., subnetwork) at 5 weeks after surgery increasing with BMS score. All MAGs within the module are shown in gray except for MAGs highlighted in blue whose VIP scores >=1 and Pearson's correlation value with BMS score >=0.45. Node sizes are correlated with VIP scores while edge widths are correlated with the strength of correlation between nodes (i.e., MAGs). This module was visualized in Cytoscape v3.7.2. **(B-C)** Heatmaps temporally show the 19 consensus PLS-VIP MAGs that change after NI at T10 and T4 spinal levels, respectively, compared to Lam. The "Ratio" annotation column refers to the ratio of median fold change at an injury level divided by median fold change at Lam to account for normal (i.e., Lam) microbiome drift over the course of the study (see "*Fold-change calculation for visualizing the PLS-VIP MAGs*" in **Methods** for details). G1: Group 1; G2: Group 2.

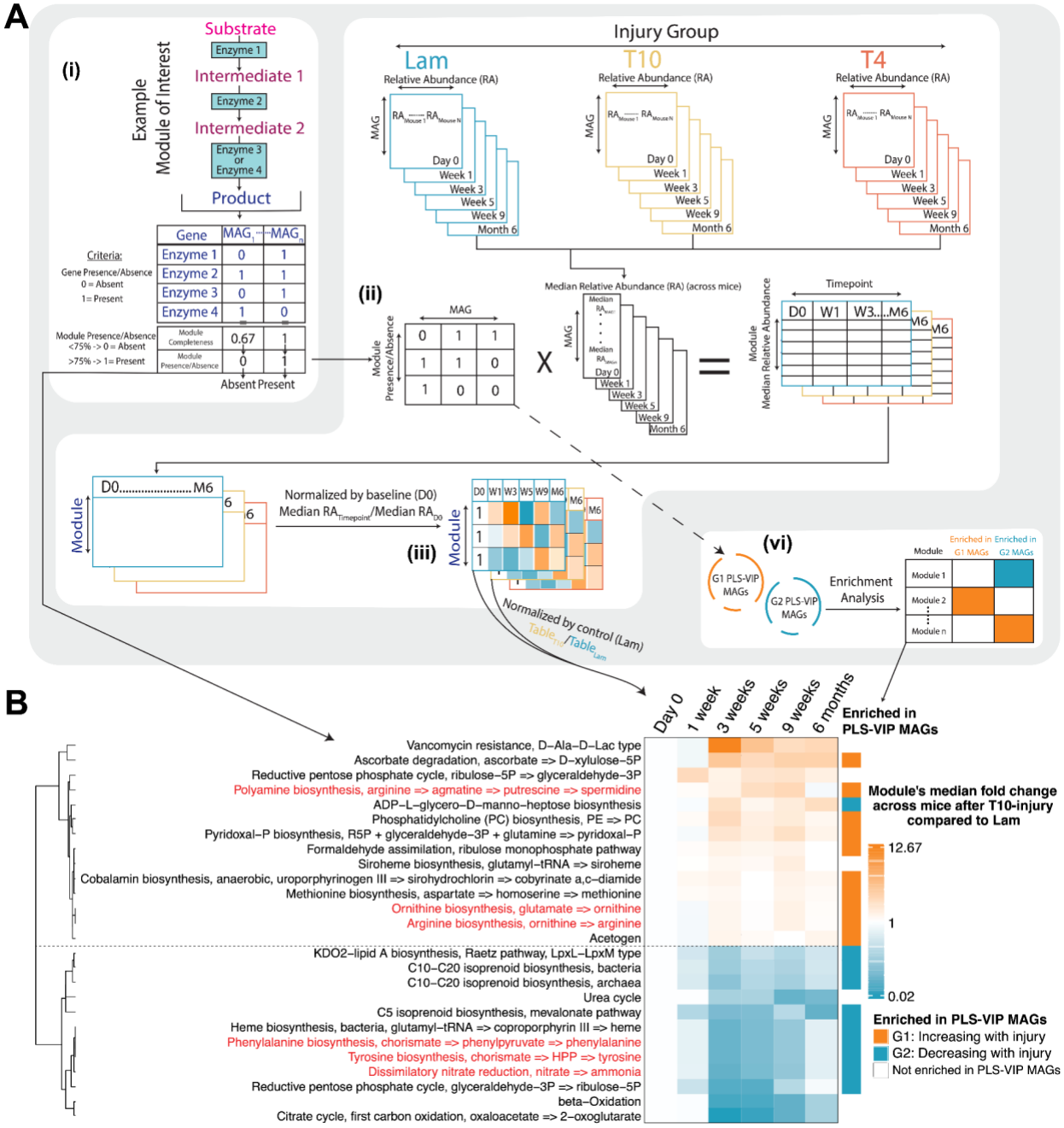

Fig. 2. Key metabolic pathways influenced by the spinal cord-gut axis. (**A**) A schematic detailing the workflow developed to determine differentially abundant PLS-VIP MAGs-driven metabolic pathways, including (i) calculating presence/absence of each pathway (i.e., KEGG modules), (ii) integrating the MAG abundance data to calculate the median relative abundance of each pathway, (iii) calculating the module's fold-change of median relative abundance per injury and across injuries, and (iv) the functional enrichment analysis performed on modules across the two groups of PLS-VIP MAGs. NI at T10 and T4 spinal levels, partially or completely, disrupts neural control over the gut. **(B)** Heatmap representing differentially abundant metabolic pathways at the community level (i.e., all de-replicated MAGs) and their enrichment in the two groups of PLS-VIP

364 MAGs caused by NI. Heatmap values indicate the ratio of median fold changes at T10
365 divided by median fold change at Lam to account for normal (i.e., Lam) microbiome drift
366 over time in male mice (see "*Fold-change calculation for visualizing pathways*" in
367 **Methods** for more details and **Fig. S2-3** for the complete representation of all pathways
368 following T10 and T4 spinal lesions for male and female mice). Pathways annotated in
369 orange are enriched in PLS-VIP MAGs that increase after NI while those in teal are
370 enriched in PLS-VIP MAGs that decrease. Red text highlights pathways discussed in this
371 report that are thought to be involved in microbial nitrogen metabolism and host nitrogen
372 balance. G1: Group 1; G2: Group 2.

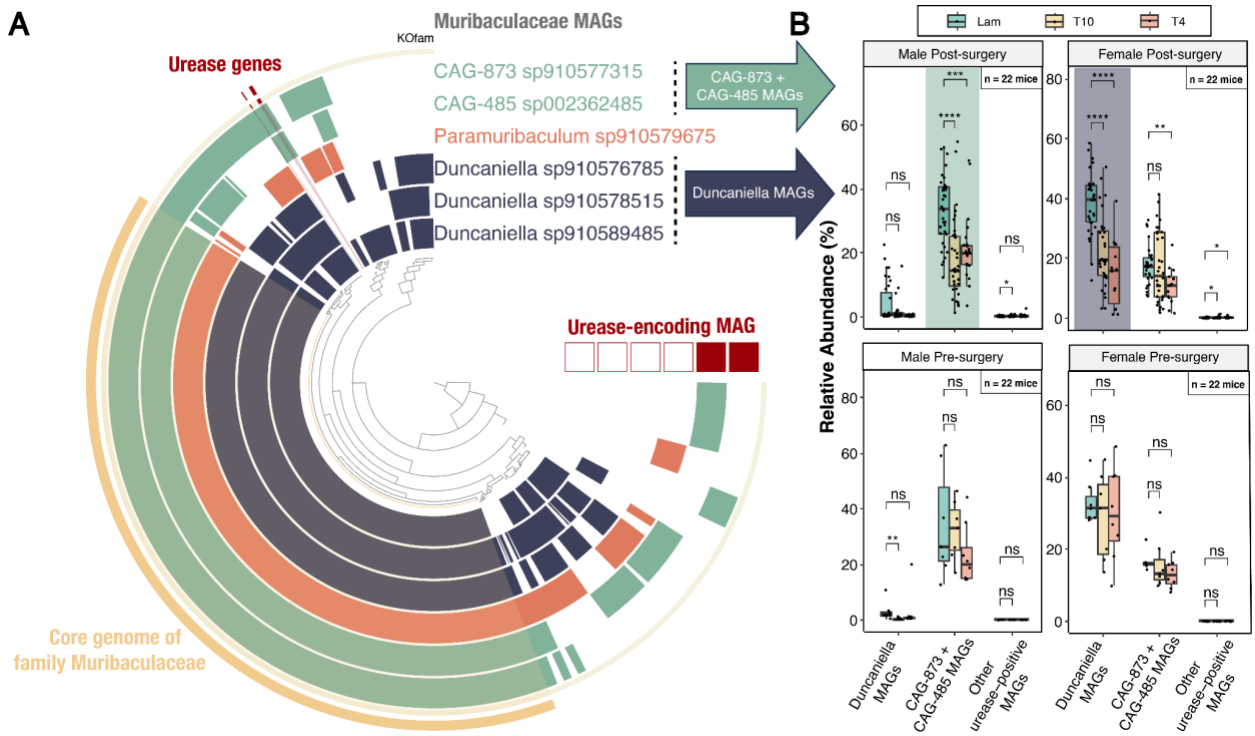

Fig. 3. Urease-encoding microbes influenced by neurological impairment. (**A**) Comparative genomics of urease-encoding MAGs within the Muribaculaceae family. MAGs belonging to the same genus are color-coded and MAGs encoding urease genes are indicated by filled red boxes. (**B**) Boxplots (with the 25th and 75th percentile ranges) of aggregate relative abundances of Muribaculaceae MAGs in male and female mice with (top) and without (bottom) NI. Peak changes are highlighted with color-shaded boxes for differentially abundant taxa in male (CAG-873 and CAG-485 MAGs) and female (Duncaniella MAGs) mice. Statistically significant differences in microbial relative abundances between treatments are indicated by the *p*-values from Wilcoxon tests. ****: $p <= 0.0001$, ***: $p <= 0.001$, **: $p <= 0.01$, *: $p <= 0.05$, ns: $p > 0.05$.

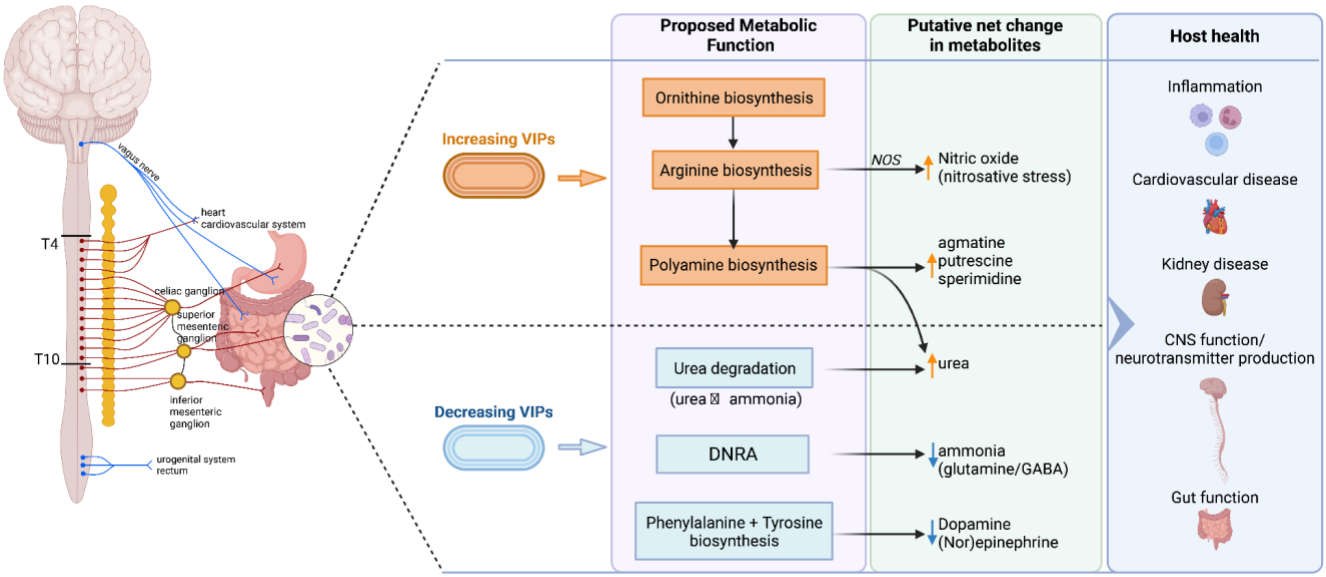

Fig. 4. Microbiota metabolic pathways impacted by neurological impairment and their potential effects on host health.
Schematic of the spinal cord-gut axis and predicted metabolic functions associated with increasing or decreasing PLS-VIP MAGs following NI. For example (see main text for expanded discussions), PLS-VIP MAGs increasing in abundance (orange) following NI result in an increase in ornithine, arginine, and polyamine biosynthesis. These, in turn, can negatively affect host health via nitrosative stress (i.e., inflammation). Conversely, decreasing PLS-VIP MAGs alter ammonia and urea metabolisms, as well as phenylalanine and tyrosine biosynthesis. A reduction in these MAGs following NI could potentially affect neurotransmitter (e.g., dopaminergic, adrenergic, and GABAergic pathways) availability required for various CNS functions.

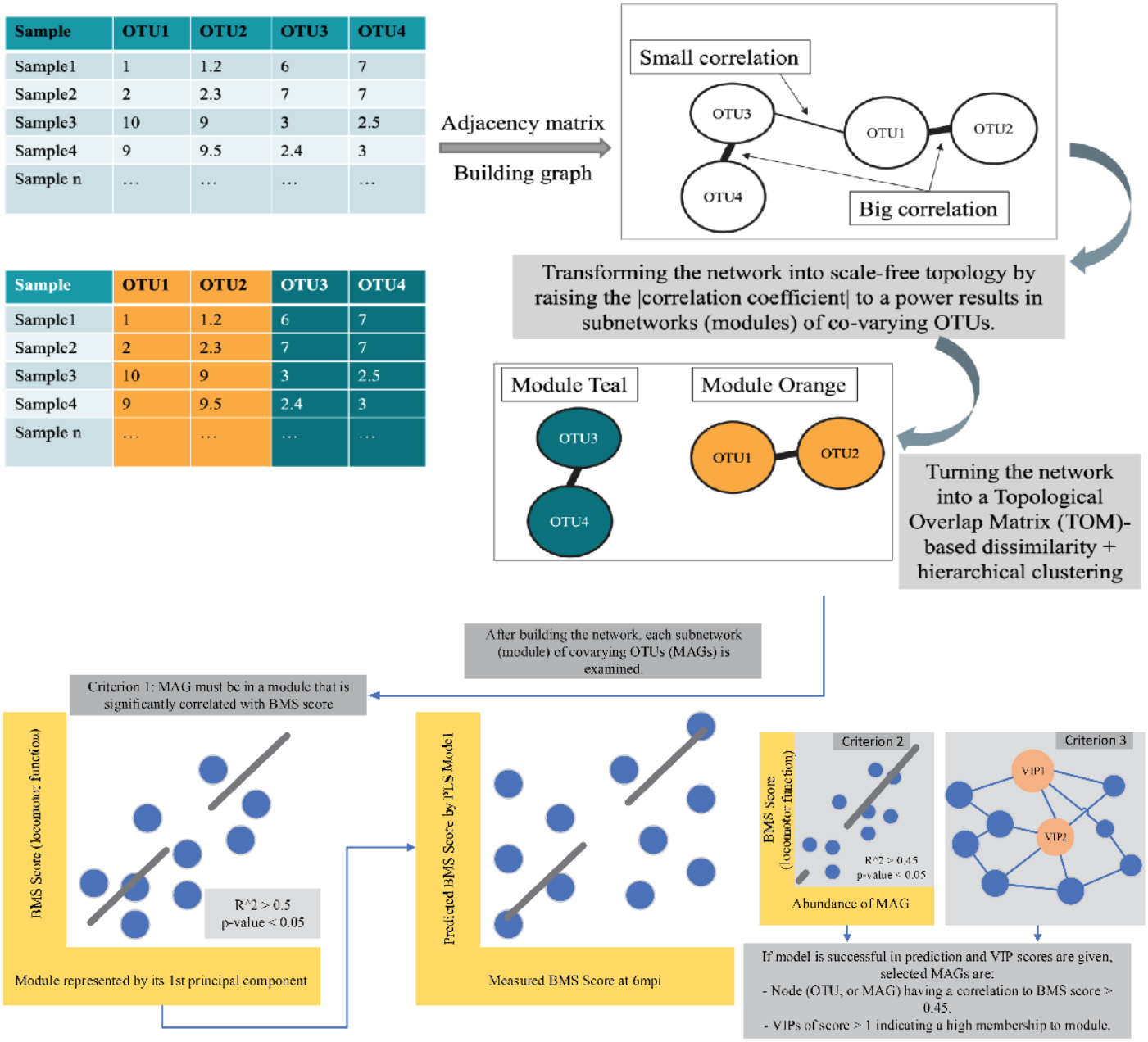

Fig. S1. Schematic showing WGCNA analysis to identify key MAGs relevant to neurological outcome after dysbiosis.

MAG abundance-based correlation networks were built separately for male and female samples for each timepoint. The workflow summarizes the steps followed for each of these individual networks (see "*WGCNA Analysis*" in **Methods** for details). First, a graph was built from MAGs (as operational taxonomic units; OTUs) relative abundances and the edges in this network were iteratively transformed (by a power-law function) to meet the scale-free topology assumption for this network. Subnetworks (or modules) from each network were then identified and individually examined across three criteria to identify PLS-VIP MAGs. First, the subnetwork is significantly

correlated (correlation coefficient of >=|0.5|, p-value <0.05) to BMS score (as a marker of injury severity). Second, cross-validated partial least squares (PLS) regression between measured and predicted BMS scores for each subnetwork identified the MAG as a key taxon driving the change in this subcommunity by the means of variable importance in projection (VIP) designation (VIP score >= 1). Third, the PLS-VIP MAG is directly or inversely correlated to BMS score using a standard correlation analysis (Pearson's correlation to BMS score >=|0.45|). Finally, consensus PLS-VIP MAGs were further selected based on manual inspection of statistical anomalies and normal (i.e., Lam) microbiome drift over time (see "*Inspection of PLS-VIP MAGs*" in **Methods** for details).

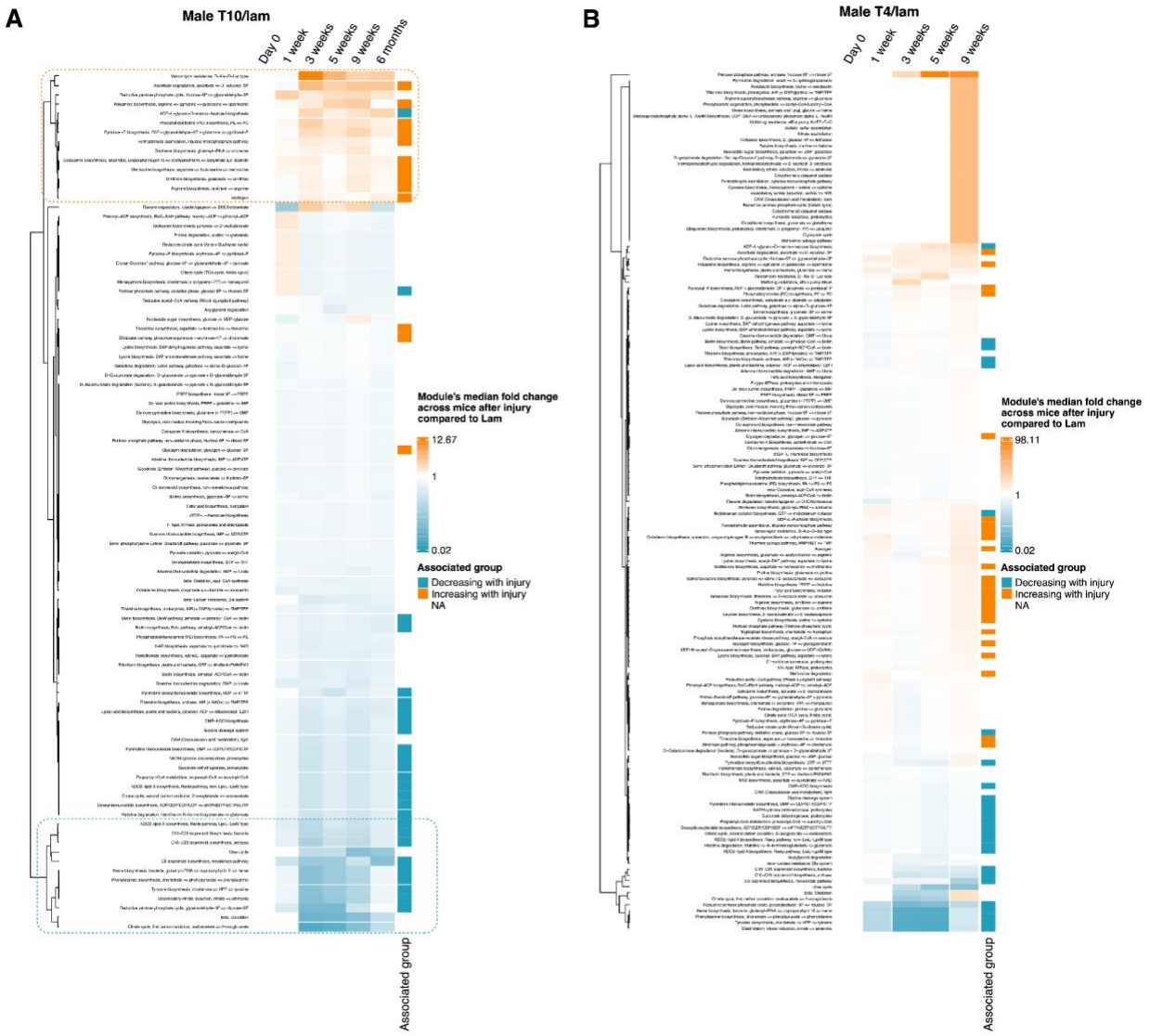

Fig. S2. Hierarchical clustering of KEGG pathway changes in male mice. KEGG pathway changes were calculated across the entire community of MAGs to provide an estimate of the overall KEGG module change in the microbiome within injury groups (**A**, T10/lam; **B**, T4/lam) and at different timepoints. Heatmap values indicate the ratio of median fold changes at T10 (**A**) or T4 (**B**) divided by median fold change at Lam to account for normal (i.e., Lam) microbiome drift over time in male mice (see "*Fold-change calculation for visualizing pathways*" in **Methods** for more details). Pathways annotated in orange are enriched in PLS-VIP MAGs that increase in mice with NI while those in teal are enriched in PLS-VIP MAGs that decrease. These modules were compared with the VIP modules from **Fig. S4B** to identify "Community VIP-driven modules" or cVIP-driven modules. The 26 modules within the top and bottom cluster of heatmap (see boxed regions in panel A) are shown in **Fig. 2B**, which represent the highest changes in T10 (panel A) and encompass all changes in T10-T4 in male (this figure) and female (**Fig. S3**) mice data.

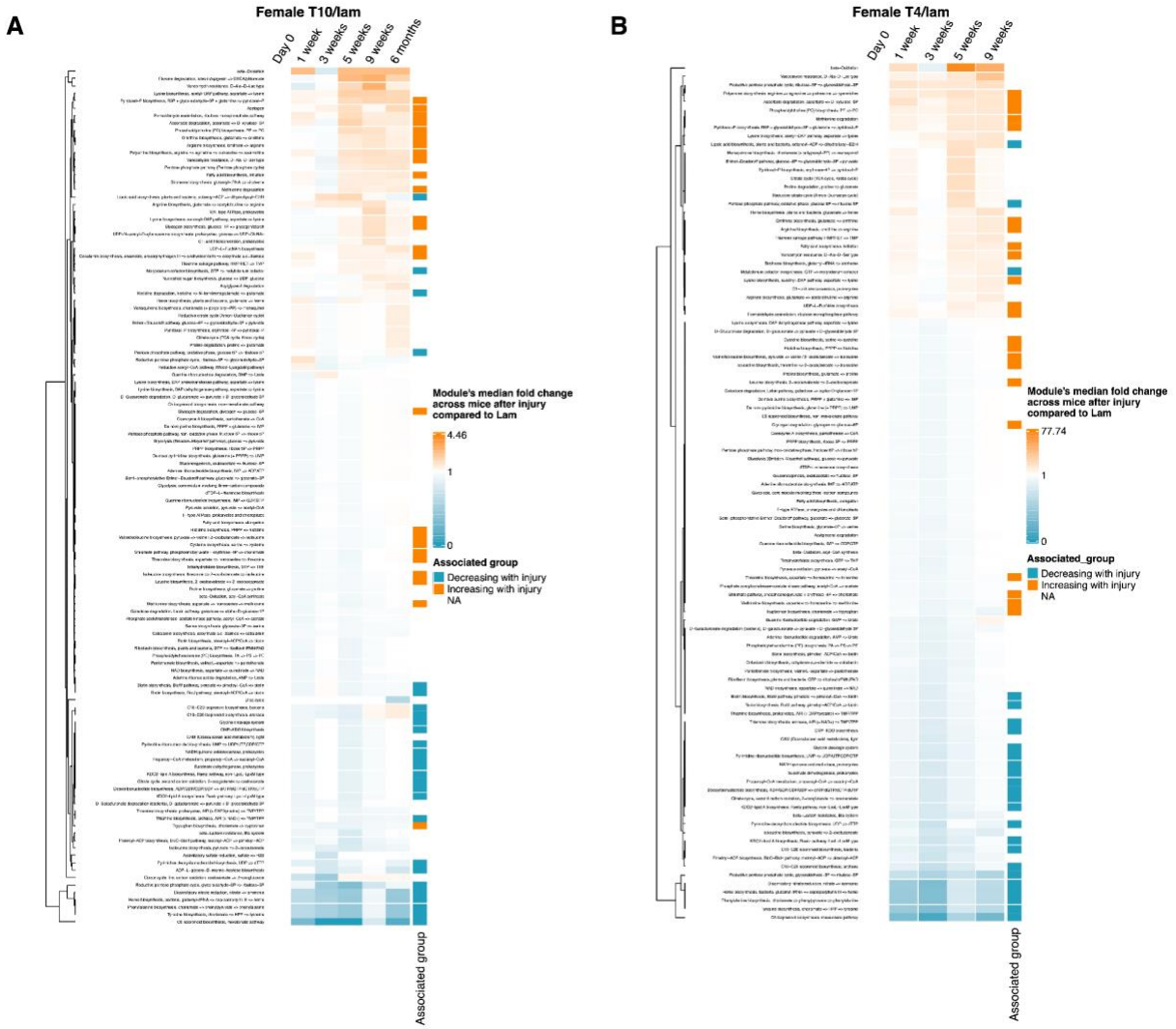

Fig. S3. Hierarchical clustering of KEGG pathway changes in female mice. KEGG pathway changes were calculated across the entire community of MAGs to provide an estimate of the overall KEGG module change in the microbiome within injury groups (**A**, T10/lam; **B**, T4/lam) and at different timepoints. Heatmap values indicate the ratio of median fold changes at T10 (**A**) or T4 (**B**) divided by median fold change at Lam to account for normal (i.e., Lam) microbiome drift over time in female mice (see "*Fold-change calculation for visualizing pathways*" in **Methods** for more details). Pathways annotated in orange are enriched in PLS-VIP MAGs that increase in mice with NI while those in teal are enriched in PLS-VIP MAGs that decrease.

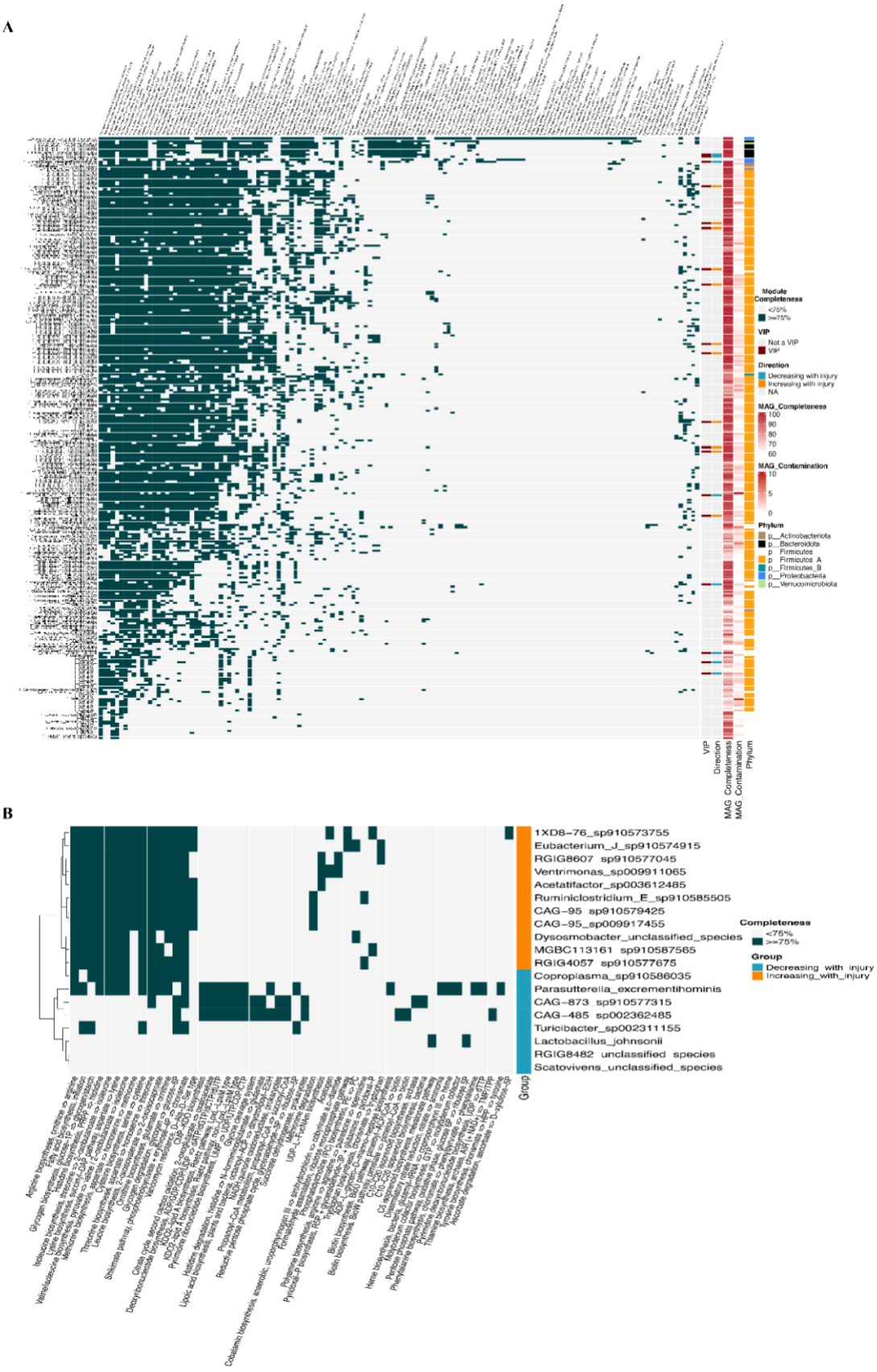
A
Module Completeness
<75%
>=75%
VIP
Not a VIP
VIP
Direction
Decreasing with injury
Increasing with injury
NA
MAG_Completeness
100
90
80
70
60
MAG_Contamination
10
5
0
Phylum
p__Actinobacteriota
p__Bacteroidota
p__Firmicutes
p__Firmicutes_A
p__Firmicutes_B
p__Proteobacteria
p__Verrucomicrobiota
VIP
Direction
MAG_Completeness
MAG_Contamination
Phylum
B
1XD8-76_sp910573755
Eubacterium_J_sp910574915
RGIG8607 sp910577045
Ventrimonas_sp009911065
Acetatifactor_sp003612485
Ruminiclostridium_E_sp910585505
CAG-95 sp910579425
CAG-95_sp009917455
Dysosmobacter_unclassified_species
MGBC113161 sp910587565
RGIG4057 sp910577675
Coproplasma_sp910586035
Parasutterella_excrementihominis
CAG-873 sp910577315
CAG-485 sp002362485
Turicibacter_sp002311155
Lactobacillus_johnsonii
RGIG8482 unclassified species
Scatovivens_unclassified_species
Group
Completeness
<75%
>=75%
Group
Decreasing_with_injury
Increasing_with_injury

440

Fig. S4. Heatmaps of KEGG modules presence-absence data of all MAGs and of PLS-VIP MAGs that change following neurological impairment.
(A) KEGG modules encoded by all 263 de-replicated MAGs. MAGs are annotated with relevant information (e.g., contamination, completeness, phylum, and whether it is a PLS-VIP MAG). **(B)** Significantly enriched KEGG modules in one of the two groups of PLS-VIP MAGs (see "*Pathway enrichment analysis*" in **Methods**). For (**A-B**), a module is considered encoded by a MAG if the MAG encodes 75% or more of the module's constituent genes.

Methods

Animals and spinal cord injury

All surgical and post-operative care procedures were performed in accordance with the Ohio State University Institutional Animal Care and Use Committee following protocol described in[19,22]. Briefly, n= 29 female C57BL/6 mice and n=30 male C57BL/6 mice from Jackson Laboratories (Bar Harbor, Maine) were used in this study. To prevent gut microbial cross-contamination due to co-habitation, all mice were single-housed. Mice were anesthetized with an intraperitoneal cocktail of ketamine (80 mg/kg)/xylazine (10 mg/kg) after which a partial laminectomy was performed at the fourth thoracic spine (T4) or the tenth thoracic spine (T10). In mice modeling SCI, modified #5 Dumont forceps were inserted laterally and held closed for 3 seconds to produce a complete crush spinal cord injury. In total, 20 mice received a complete crush at T4, 20 mice received a complete crush at T10, and 19 mice received laminectomy (Lam) only.

Fecal samples for metagenomic sequencing were aseptically collected pre-injury, 1-week, 2-weeks, 3-weeks, 5-weeks, 9-weeks, and 6-months post-injury, immediately frozen and stored at -80°C.

WGCNA analysis

To identify key MAGs, or species, driving dysbiosis in the microbial community from a healthy state (i.e., Lam mice) to a diseased state (i.e., T10- or T4-injured mice), co-occurrence networks were built with hellinger-transformed MAG abundances using the "decostand" function from the R package "vegan" (https://github.com/vegandevs/vegan). These networks were built under the framework of WGCNA[80] (R package: https://cran.r-project.org/web/packages/WGCNA/index.html), a systems biology approach used to detect significant associations between genes or taxa and a system variable (BMS-score of mice at 6-months post injury in this study). This continuous variable accounts for incomplete injuries or partial crushing of the spinal cord rather than using a categorical variable such as injury levels. Here, WGCNA was used on male and female cohorts separately, and one network was built per each timepoint. All codes used were deposited in the accompanying Zenodo repository.

For building networks: Hellinger-transformed abundance tables were used to build the networks using the biweight midcorrelation method (corType="bicor"). The values used as soft thresholds to ensure the networks' free-scale topology were 10, 12, 12, 14, 16, and 18 for pre-injury (i.e., baseline, or Day 0), 1 week, 3 weeks, 5 weeks, 9 weeks, and 6 months post-injury, respectively. The corresponding values for female mice data were 10, 12, 14, 14, 10, 14. Networks were built by the blockwiseModules function in the WGCNA package, requiring the "signed" option for both networkType and TOMType, and a minimum module size of 15.

Finding modules significantly correlated to BMS score: For each subnetwork, or module, of covarying MAGs extracted from each network (e.g. per timepoint in males), pairwise Pearson's correlation coefficients and their corresponding *p*-values were calculated between the

module's first principal component and the BMS score. A module was considered significant if it has a correlation coefficient of |0.5| or larger and a *p*-value of less than 0.05. The modules with the highest correlation scores were examined further. These included two modules at 1 week, three at 3 weeks, two at 5 weeks, three at 9 weeks, and one at 6 months. No modules with significant correlation were found at Day 0, corroborating that there were no baseline pre-injury differences. All significant modules and their correlation coefficients and *p*-values are shown in **Fig. 1A**.

PLS-VIP MAGs selection: To identify taxa driving changes per module, we applied partial least squares (PLS) regression to determine the best predictors of BMS score. This was validated by a machine learning, leave-one-out cross-validation (LOOCV) method. All predictors per module were ranked according to their contribution in the PLS regression, which is known as their variable importance in projection (VIP). MAGs with larger than |0.45| Pearson's correlation to BMS score that also had a VIP score larger than 1 were considered important for the PLS prediction and were thus further investigated. We refer to these MAGs as "PLS-VIP MAGs" throughout the manuscript (or "VIPs" for short).

Inspection of PLS-VIP MAGs: To identify "consensus" PLS-VIP MAGs, each MAG was tested a) temporally within each treatment (i.e., injury levels) and b) across treatments per each timepoint, both using pairwise wilcoxon tests as described above. Unless otherwise stated (see full rationale for the selection criteria for each MAG in the accompanying Zenodo repository), PLS-VIP MAGs were kept in the "consensus" list if: a) their abundances significantly changed over time in T10 and/or T4 mice compared to baseline (Day0) when testing was constrained by treatment; and b) their abundances significantly changed between Lam (control) and T10 or Lam and T4 at one or more timepoints when testing was constrained by timepoint. In both testing strategies, trends in control samples (e.g., significant changes in Lam over time) and at baseline (e.g., significant changes in T10 or T4 compared to Lam at Day0) were used to inform exclusion from the consensus list.

Fold-change calculation for visualizing the PLS-VIP MAGs

In each mouse, the MAG's relative abundance at each timepoint was divided by its relative abundance at Day 0 after introducing small pseudo-counts (both quantities were multiplied by 1000 and added to 1) to avoid division by zero. The median fold-changes across mice was calculated for each taxon per injury and timepoint. The median fold-changes in T10 or T4 were then divided over those in Lam for each taxon and then plotted. The heatmaps (**Fig. 1B-C**) were constructed with the ComplexHeatmap package[81] (https://github.com/jokergoo/ComplexHeatmap) and all values were log2-transformed to improve color ranges.

Pathway identification

Using Anvi'o v7.1 (https://github.com/merenlab/anvio) and all de-replicated MAGs as external genomes, the following commands were used with their default parameters on each MAG: anvi-gen-contigs-database, anvi-run-hmms, anvi-run-kegg-kofams, and anvi-estimate-metabolism (with --kegg-output-modes modules, kofam hits and --matrix-format). This gives identified KEGG modules and KO hits per MAG as well as module completeness and presence-absence matrices per MAG. The default value (75%) for module completeness was used.

Pathway enrichment analysis

Using Anvi'o v7.1 and the PLS-VIP MAGs as external genomes, the anvi-compute-metabolic-enrichment function was used to compute enrichment in the 2 groups of PLS-VIP MAGs (i.e., the ones enriched in T10 or T4 compared to Lam and the ones enriched in Lam compared to these two injuries). KEGG modules with an adjusted *q*-value of less than 0.05 or ones that are present in one group while absent in the other were considered and plotted in **Fig. S4B**.

Fold-change calculation for visualizing pathways

The abundance of a KEGG module (i.e., pathway) was calculated from the total of the abundances of the MAGs encoding it. First, the median abundance of each MAG across all mice per sex, injury, and timepoint was calculated. Next, this median abundance was multiplied by the presence-absence value of the KEGG Module (1 or zero) determined by Anvi'o as explained above, where a module is considered present if it is at least 75% complete. These quantities (median MAG abundance across mice belonging to the same injury and timepoint, multiplied by the module's presence/absence value) were then summed for all MAGs to give an estimate of the overall KEGG module's abundance per sex, injury and timepoint. For each sex, these values at each timepoint, per injury, were then divided by the values at Day0 to calculate the median fold change. Finally, T10 and T4 values were divided by the corresponding Lam values. Heatmaps (**Fig. 2B** and **Fig. S2-3**) were constructed with the ComplexHeatmap package and all values were log10-transformed to improve color ranges.

Data availability

All data produced in this study are publicly available. Curated data and all used codes and databases can be found in the following Zenodo DOI: 10.5281/zenodo.15613780 (unpublished until review is completed).

Acknowledgements

We appreciate the help and support from all members of the Popovich and Sullivan laboratories, especially Natalie Solonenko, who participated in data sequencing, and Ami Fofana for her immense help with visual representations. We'd also like to acknowledge the Center of Microbiome Science, Ohio Supercomputer Center, and the Riffomonas educational resource[82]. This work is funded by a National Institutes of Neurological Disorders and Stroke R35 award (grant no. 1R35NS111582) to P.G.P., The Belford Center for Spinal Cord Injury (P.G.P.), The Ray W. Poppleton Research designated endowment (P.G.P.), a Craig H. Nielsen Foundation Senior Research award (grant no. 890085) to K.A.K, and NSF awards ABI#2149505 and DBI#2022070 to M.B.S.

Author Contributions

P.G.P., M.B.S., K.A.K., A.A.Z. conceived the project and experimental design. P.G.P., M.B.S., K.A.K., A.A.Z., and M.M. developed the data analysis plan. P.G.P., M.B.S., K.A.K., A.A.Z., M.M., G.J.S., J.D., and J.M.S. helped with data interpretation and writing of the manuscript. M.M. performed the statistical, functional, bioinformatic, and eco-systems biology analyses, and managed and coordinated responsibilities for the manuscript preparation. A.A.Z. guided and supervised statistical, functional, and bioinformatic analyses, performed eco-systems biology analyses, co-developed the WGCNA pipeline, and drafted the manuscript with M.M.. M.M., K.A.K., A.A.Z., and G.J.S. contributed to figure generation and, with P.G.P., contributed to improving illustrations. G.J.S. guided functional analyses. All authors read and reviewed the manuscript and approved it in its final form.

Declaration of interests

All authors declare no competing interest.

Declaration of generative AI and AI-assisted technologies

During preparation of this work, Microsoft CoPilot and ChatGPT were used periodically to improve writing or shorten passages. After using it, the authors reviewed and edited the content as needed and take full responsibility for the content of the publication.

603

604 # References

605

606 1. Moran, M. A. *et al.* Microbial metabolites in the marine carbon cycle. *Nat Microbiol* **7**, 508–
607 523 (2022).
608 2. Schimel, J. P. & Schaeffer, S. M. Microbial control over carbon cycling in soil. *Front*
609 *Microbiol* **3**, 348 (2012).
610 3. Kuypers, M. M. M., Marchant, H. K. & Kartal, B. The microbial nitrogen-cycling network.
611 *Nat Rev Microbiol* **16**, 263–276 (2018).
612 4. Valido, E. *et al.* Systematic review of the changes in the microbiome following spinal cord
613 injury: animal and human evidence. *Spinal Cord* **60**, 288–300 (2022).
614 5. Hou, K. *et al.* Microbiota in health and diseases. *Signal Transduct Target Ther* **7**, 135 (2022).
615 6. Sorboni, S. G., Moghaddam, H. S., Jafarzadeh-Esfehani, R. & Soleimanpour, S. A
616 Comprehensive Review on the Role of the Gut Microbiome in Human Neurological
617 Disorders. *Clin Microbiol Rev* **35**, e0033820 (2022).
618 7. Gohl, D. M. *et al.* Systematic improvement of amplicon marker gene methods for increased
619 accuracy in microbiome studies. *Nat Biotechnol* **34**, 942–949 (2016).
620 8. Bonk, F., Popp, D., Harms, H. & Centler, F. PCR-based quantification of taxa-specific
621 abundances in microbial communities: Quantifying and avoiding common pitfalls. *J*
622 *Microbiol Methods* **153**, 139–147 (2018).
623 9. Coleman, M. L. & Chisholm, S. W. Code and context: Prochlorococcus as a model for cross-
624 scale biology. *Trends Microbiol* **15**, 398–407 (2007).
625 10. Lesker, T. R. *et al.* An Integrated Metagenome Catalog Reveals New Insights into the
626 Murine Gut Microbiome. *Cell Rep* **30**, 2909-2922.e6 (2020).

627 11. Arevalo, P., VanInsberghe, D., Elsherbini, J., Gore, J. & Polz, M. F. A Reverse Ecology
628 Approach Based on a Biological Definition of Microbial Populations. *Cell* **178**, 820-834.e14
629 (2019).
630 12. Kim, N. *et al.* Genome-resolved metagenomics: a game changer for microbiome medicine.
631 *Exp Mol Med* **56**, 1501–1512 (2024).
632 13. Eren, A. M. & Banfield, J. F. Modern microbiology: Embracing complexity through
633 integration across scales. *Cell* **187**, 5151–5170 (2024).
634 14. Chen, L. *et al.* Gut microbial co-abundance networks show specificity in inflammatory
635 bowel disease and obesity. *Nat Commun* **11**, 4018 (2020).
636 15. Bäumler, A. J. & Sperandio, V. Interactions between the microbiota and pathogenic bacteria
637 in the gut. *Nature* **535**, 85–93 (2016).
638 16. Kim, T. J. *et al.* Optimizing Nitrogen Balance Is Associated with Better Outcomes in
639 Neurocritically Ill Patients. *Nutrients* **12**, 3137 (2020).
640 17. Fuller, M. F. & Reeds, P. J. Nitrogen cycling in the gut. *Annu Rev Nutr* **18**, 385–411 (1998).
641 18. Stewart, G. S. & Smith, C. P. Urea nitrogen salvage mechanisms and their relevance to
642 ruminants, non-ruminants and man. *Nutr Res Rev* **18**, 49–62 (2005).
643 19. Du, J. *et al.* Spinal Cord Injury Changes the Structure and Functional Potential of Gut
644 Bacterial and Viral Communities. *mSystems* **6**, e01356-20 (2021).
645 20. Taraskina, A. *et al.* Effects of Traumatic Brain Injury on the Gut Microbiota Composition
646 and Serum Amino Acid Profile in Rats. *Cells* **11**, 1409 (2022).
647 21. Dionyssiotis, Y., Papachristos, A., Petropoulou, K., Papathanasiou, J. & Papagelopoulos, P.
648 Nutritional Alterations Associated with Neurological and Neurosurgical Diseases. *Open*
649 *Neurol J* **10**, 32–41 (2016).

650 22. The Spinal Cord-Gut Axis Regulates Gut Microbial Homeostasis: Insights from a New
651 Murine Metagenomic Catalog | bioRxiv.
652 https://www.biorxiv.org/content/10.1101/2025.05.27.656368v1.abstract.
653 23. Basso, D. M. *et al.* Basso Mouse Scale for locomotion detects differences in recovery after
654 spinal cord injury in five common mouse strains. *J Neurotrauma* **23**, 635–659 (2006).
655 24. Guidi, L. *et al.* Plankton networks driving carbon export in the oligotrophic ocean. *Nature*
656 **532**, 465–470 (2016).
657 25. Zhang, B. & Horvath, S. A general framework for weighted gene co-expression network
658 analysis. *Stat Appl Genet Mol Biol* **4**, Article17 (2005).
659 26. Bai, Y. *et al.* Lactobacillus johnsonii enhances the gut barrier integrity via the interaction
660 between GAPDH and the mouse tight junction protein JAM-2. *Food Funct* **13**, 11021–11033
661 (2022).
662 27. Jia, D.-J.-C. *et al.* Lactobacillus johnsonii alleviates colitis by TLR1/2-STAT3 mediated
663 CD206+ macrophagesIL-10 activation. *Gut Microbes* **14**, 2145843 (2022).
664 28. Zhu, H. *et al.* Cholesterol-lowering effect of bile salt hydrolase from a Lactobacillus
665 johnsonii strain mediated by FXR pathway regulation. *Food Funct* **13**, 725–736 (2022).
666 29. Feng, C. *et al.* Dynamic Changes of the Gut Microbiota and Its Functional Metagenomic
667 Potential during the Development of Non-Small Cell Lung Cancer. *Int J Mol Sci* **25**, 3768
668 (2024).
669 30. Lynch, J. B. *et al.* Gut microbiota Turicibacter strains differentially modify bile acids and
670 host lipids. *Nat Commun* **14**, 3669 (2023).

671 31. Ju, T., Kong, J. Y., Stothard, P. & Willing, B. P. Defining the role of Parasutterella, a
672 previously uncharacterized member of the core gut microbiota. *ISME J* **13**, 1520–1534
673 (2019).
674 32. Forster, S. C. *et al.* Identification of gut microbial species linked with disease variability in a
675 widely used mouse model of colitis. *Nat Microbiol* **7**, 590–599 (2022).
676 33. Künstner, A., Schilf, P., Busch, H., Ibrahim, S. M. & Hirose, M. Changes of Gut Microbiota
677 by Natural mtDNA Variant Differences Augment Susceptibility to Metabolic Disease and
678 Ageing. *Int J Mol Sci* **23**, 1056 (2022).
679 34. Saravi, S. S. S. *et al.* Gut microbiota-dependent increase in phenylacetic acid induces
680 endothelial cell senescence during aging. 2023.11.17.567594 Preprint at
681 https://doi.org/10.1101/2023.11.17.567594 (2023).
682 35. Moya, A. & Ferrer, M. Functional Redundancy-Induced Stability of Gut Microbiota
683 Subjected to Disturbance. *Trends Microbiol* **24**, 402–413 (2016).
684 36. Tian, L. *et al.* Deciphering functional redundancy in the human microbiome. *Nat Commun*
685 **11**, 6217 (2020).
686 37. Culp, E. J. & Goodman, A. L. Cross-feeding in the gut microbiome: Ecology and
687 mechanisms. *Cell Host Microbe* **31**, 485–499 (2023).
688 38. Eren, A. M. *et al.* Community-led, integrated, reproducible multi-omics with anvi'o. *Nat*
689 *Microbiol* **6**, 3–6 (2021).
690 39. Veseli, I. *et al.* Microbes with higher metabolic independence are enriched in human gut
691 microbiomes under stress. *bioRxiv* 2023.05.10.540289 (2024)
692 doi:10.1101/2023.05.10.540289.

40. Shaiber, A. *et al.* Functional and genetic markers of niche partitioning among enigmatic members of the human oral microbiome. *Genome Biol* **21**, 292 (2020).

41. Kraft, B., Strous, M. & Tegetmeyer, H. E. Microbial nitrate respiration – Genes, enzymes and environmental distribution. *Journal of Biotechnology* **155**, 104–117 (2011).

42. Jones, G. A. Dissimilatory metabolism of nitrate by the rumen microbiota. *Can J Microbiol* **18**, 1783–1787 (1972).

43. Allison, C. & Macfarlane, G. T. Effect of nitrate on methane production and fermentation by slurries of human faecal bacteria. *J Gen Microbiol* **134**, 1397–1405 (1988).

44. The Dissimilatory Reduction of Nitrate to Ammonia by Anaerobic Bacteria - ScienceDirect. https://www.sciencedirect.com/science/article/abs/pii/B9780444528575500084?via%3Dihub .

45. Vermeiren, J., Van de Wiele, T., Verstraete, W., Boeckx, P. & Boon, N. Nitric oxide production by the human intestinal microbiota by dissimilatory nitrate reduction to ammonium. *J Biomed Biotechnol* **2009**, 284718 (2009).

46. Wang, P. *et al.* Gut microbiome-derived ammonia modulates stress vulnerability in the host. *Nat Metab* **5**, 1986–2001 (2023).

47. Douglas, G. M. *et al.* PICRUSt2 for prediction of metagenome functions. *Nat Biotechnol* **38**, 685–688 (2020).

48. Carr, A., Diener, C., Baliga, N. S. & Gibbons, S. M. Use and abuse of correlation analyses in microbial ecology. *ISME J* **13**, 2647–2655 (2019).

49. Temporal dynamics and network analysis - Blonder - 2012 - Methods in Ecology and Evolution - Wiley Online Library. https://besjournals.onlinelibrary.wiley.com/doi/10.1111/j.2041-210X.2012.00236.x.

716 50. Lorenzi, R. M. *et al.* Unsuspected Involvement of Spinal Cord in Alzheimer Disease. *Front*
717 *Cell Neurosci* **14**, 6 (2020).
718 51. Emmenegger, T. M. *et al.* Progressive cervical cord atrophy parallels cognitive decline in
719 Alzheimer's disease. *Sci Rep* **14**, 21595 (2024).
720 52. Del Tredici, K. & Braak, H. Spinal cord lesions in sporadic Parkinson's disease. *Acta*
721 *Neuropathol* **124**, 643–664 (2012).
722 53. Kreiter, D., Postma, A. A., Hupperts, R. & Gerlach, O. Hallmarks of spinal cord pathology in
723 multiple sclerosis. *J Neurol Sci* **456**, 122846 (2024).
724 54. Saberi, S., Stauffer, J. E., Schulte, D. J. & Ravits, J. Neuropathology of Amyotrophic Lateral
725 Sclerosis and Its Variants. *Neurol Clin* **33**, 855–876 (2015).
726 55. Karbasforoushan, H., Cohen-Adad, J. & Dewald, J. P. A. Brainstem and spinal cord MRI
727 identifies altered sensorimotor pathways post-stroke. *Nat Commun* **10**, 3524 (2019).
728 56. Irvine, K.-A., Sahbaie, P., Liang, D.-Y. & Clark, J. D. Traumatic Brain Injury Disrupts Pain
729 Signaling in the Brainstem and Spinal Cord. *J Neurotrauma* **35**, 1495–1509 (2018).
730 57. Assessment of sex differences in serum urea and creatinine levels following an acute spinal
731 cord injury in albino rat models | Bayero Journal of Medical Laboratory Science.
732 https://www.ajol.info/index.php/bjmls/article/view/222018.
733 58. Rodriguez, D. J., Clevenger, F. W., Osler, T. M., Demarest, G. B. & Fry, D. E. Obligatory
734 negative nitrogen balance following spinal cord injury. *JPEN J Parenter Enteral Nutr* **15**,
735 319–322 (1991).
736 59. Thibault-Halman, G., Casha, S., Singer, S. & Christie, S. Acute management of nutritional
737 demands after spinal cord injury. *J Neurotrauma* **28**, 1497–1507 (2011).

738 60. Harris, A. N. *et al.* Differences in renal ammonia metabolism in male and female kidney. *Am*
739 *J Physiol Renal Physiol* **315**, F211–F222 (2018).
740 61. Harris, A. N., Castro, R. A., Lee, H.-W., Verlander, J. W. & Weiner, I. D. Role of the renal
741 androgen receptor in sex differences in ammonia metabolism. *Am J Physiol Renal Physiol*
742 **321**, F629–F644 (2021).
743 62. Gonzalez-Lopez, E. & Vrana, K. E. Dopamine beta-hydroxylase and its genetic variants in
744 human health and disease. *J Neurochem* **152**, 157–181 (2020).
745 63. Wu, G. & Morris, S. M. Arginine metabolism: nitric oxide and beyond. *Biochem J* **336 (Pt**
746 **1)**, 1–17 (1998).
747 64. McRae, M. P. Therapeutic Benefits of l-Arginine: An Umbrella Review of Meta-analyses. *J*
748 *Chiropr Med* **15**, 184–189 (2016).
749 65. Kasahara, N. *et al.* Dietary polyamines promote intestinal adaptation in an experimental
750 model of short bowel syndrome. *Sci Rep* **14**, 4605 (2024).
751 66. Erens, C. *et al.* L-Arginine Depletion Improves Spinal Cord Injury via Immunomodulation
752 and Nitric Oxide Reduction. *Biomedicines* **10**, 205 (2022).
753 67. Erens, C., Van Broeckhoven, J., Bronckaers, A., Lemmens, S. & Hendrix, S. The Dark Side
754 of an Essential Amino Acid: L-Arginine in Spinal Cord Injury. *J Neurotrauma* **40**, 820–832
755 (2023).
756 68. Saito, A., Takagi, T., Chung, T. G. & Ohta, K. Serum levels of polyamines in patients with
757 chronic renal failure. *Kidney Int Suppl* **16**, S234-237 (1983).
758 69. Piletz, J. E. *et al.* Agmatine: clinical applications after 100 years in translation. *Drug Discov*
759 *Today* **18**, 880–893 (2013).

760 70. Saha, P. *et al.* Neuroprotection by agmatine: Possible involvement of the gut microbiome?
761 *Ageing Research Reviews* **91**, 102056 (2023).
762 71. Fischbach, M. A. & Sonnenburg, J. L. Eating for two: how metabolism establishes
763 interspecies interactions in the gut. *Cell Host Microbe* **10**, 336–347 (2011).
764 72. Beresford-Jones, B. S. *et al.* The Mouse Gastrointestinal Bacteria Catalogue enables
765 translation between the mouse and human gut microbiotas via functional mapping. *Cell Host*
766 *Microbe* **30**, 124-138.e8 (2022).
767 73. Liu, C. *et al.* The Mouse Gut Microbial Biobank expands the coverage of cultured bacteria.
768 *Nat Commun* **11**, 79 (2020).
769 74. Giampazolias, E. *et al.* Vitamin D regulates microbiome-dependent cancer immunity.
770 *Science* **384**, 428–437 (2024).
771 75. Pruss, K. M. *et al.* Host-microbe co-metabolism via MCAD generates circulating metabolites
772 including hippuric acid. *Nat Commun* **14**, 512 (2023).
773 76. Wilde, J., Slack, E. & Foster, K. R. Host control of the microbiome: Mechanisms, evolution,
774 and disease. *Science* **385**, eadi3338 (2024).
775 77. van Leeuwen, P. T., Brul, S., Zhang, J. & Wortel, M. T. Synthetic microbial communities
776 (SynComs) of the human gut: design, assembly, and applications. *FEMS Microbiol Rev* **47**,
777 fuad012 (2023).
778 78. Raghu, A. K., Palanikumar, I. & Raman, K. Designing function-specific minimal
779 microbiomes from large microbial communities. *NPJ Syst Biol Appl* **10**, 46 (2024).
780 79. Quinn-Bohmann, N., Carr, A. V., Diener, C. & Gibbons, S. M. Moving from genome-scale
781 to community-scale metabolic models for the human gut microbiome. *Nat Microbiol* **10**,
782 1055–1066 (2025).

783 80. Langfelder, P. & Horvath, S. WGCNA: an R package for weighted correlation network
784 analysis. *BMC Bioinformatics* **9**, 559 (2008).
785 81. Gu, Z. Complex heatmap visualization. *Imeta* **1**, e43 (2022).
786 82. Schloss, P. D. The Riffomonas YouTube Channel: An Educational Resource To Foster
787 Reproducible Research Practices. *Microbiol Resour Announc* **12**, e0131022 (2023).